coatings

MDPI

Article

Influence of Inter-Particle Bonding on Compression Performance of Porous Mo Deposited by Flame Spraying of Semi-Molten Particles

Jiantao Yao *, Hui Dong, Yan Li and Xiao Li

School of Materials Science and Engineering, Xi'an Shiyou University, Xi'an 710065, China; donghui@xsyu.edu.cn (H.D.); yli@xsyu.edu.cn (Y.L.); xli@xsyu.edu.cn (X.L.)

* Correspondence: jiantaoyao@xsyu.edu.cn or jiantao.yao@163.com; Tel.: +86-29-8838-2607

Received: 28 December 2018; Accepted: 26 February 2019; Published: 28 February 2019

Abstract: A novel method has been proposed to prepare porous materials through deposition of semi-molten particles by flame spraying. In this study, it was found that the porous material was deposited by the stacking of semi-molten particles which were welded by the molten fraction to form a large and strong inter-particle bonding neck between deposited particles. In order to reveal the effect of inter-particle bonding on the compressive behavior of porous Mo, the deposits were investigated by altering the bonding through vacuum sintering of porous Mo with different porosities. Results showed that the sintering temperature and time influenced the bonding significantly and subsequently influenced the properties of flame-sprayed porous Mo deposits. The oxides formed during flame spraying were effectively reduced under hydrogen atmosphere. In addition, the inter-particle bonding and compressive properties of flame-sprayed porous Mo were significantly improved by optimizing the sintering temperature and the heat treatment time.

Keywords: flame spraying; semi-molten particles; inter-particle bonding; compression property

1. Introduction

As structural function materials, porous metallic materials have attracted wide attention. The mechanical, electromagnetic, thermal, and physical properties of porous materials are significantly affected by their structure [1–4]. Molybdenum is extensively applied in the aerospace and power industries due to its excellent thermo-mechanical properties [5]. However, the applications of Mo are limited due to processing difficulties resulting from its high melting point (2600 ± 50 °C). A conventional processing method to fabricate porous Mo is powder metallurgy processing [6,7]. However, the low porosity (below 30%) achieved by this method cannot meet application requirements. Recently, porous Mo with 68% porosity was fabricated through the deposition of semi-molten Mo particles by using flame spraying as the skeleton for an Mo-Cu composite [8]. However, mechanical properties have been found to deteriorate with increases in the porosity of porous materials [9]. In order to ensure deformation behavior of porous Mounder various stress conditions, its compression performance should be investigated. Compression performance is one of the most important indicators of the mechanical properties of porous materials [10,11]. However, there is still no uniform standard to evaluate the compression performance of porous metallic materials.

As has been widely recognized, the mechanical properties of porous metallic materials are not only affected by the material itself but also by the microstructure of the material, including the porosity as well as the distribution and morphology of the pores. Generally, the deformation of metal porous materials has been presented as a process of plastic yield deformation and gradual densification [12,13]. For porous metallic materials of the same density, the elastic modulus of the

material with a closed pore structure is evidently higher than that of the material with an open pore structure. This is because porous metal materials with different pore structures have different deformation mechanisms. In porous materials with open pore structures, the compressive deformation occurs in the neck; in porous materials with closed pore structures, the deformation occurs in the wall around the poles [14–16]. The compressive properties of porous materials of different types and structures have been reviewed systematically by researchers. Studies have shown that the compressive properties of porous metal materials decrease with increases in porosity [17]. The compression process of porous metal material clearly consists of three stages: the elastic deformation stage, the deformation plateau stage, and the densification stage. The elastic deformation stage reflects the elastic modulus and the compressive yield strength. The deformation plateau stage depends on the maximum compressive yield strength and the corresponding strain, and it represents the energy absorption characteristics of porous metal materials.

However, porous materials prepared by selective laser sintering, such as porous 316L, have directional pore structures and low compressive yield strengths, and the compression curves have no obvious yield platform area. Fabrication of porous materials by powder sintering involves the formation of necks between the powders by high temperature diffusion [18–21]. Therefore, the prepared porous materials exhibit poor mechanical properties and corrosion resistance. To sum up, the bonding of particles has a significant effect on the compressive properties of porous materials. According to previous studies, metal particles are oxidized during flame spraying and metal oxides can be reduced after heat treatment in a reducing atmosphere. In addition, heat treatment significantly improves the bonding strength between particles [22,23]. However, for porous metallic materials prepared by depositing semi-molten particles, the relationships between the microstructures and properties, as well as the influence of the oxide on the mechanical properties, are still not clear.

In the present study, porous Mo deposits were fabricated through depositing semi-molten particles by flame spraying. The as-sprayed deposits were then subjected to reduction treatment in an H_2 atmosphere to reduce the oxides. Subsequently, the deposits were sintered in a vacuum furnace to improve the bonding between the particles of porous Mo. Variation in the microstructure of porous Mo was characterized to understand the effect of inter-particle bonding on the compressive behavior of flame-sprayed porous Mo. Based on the results, the relationship between the inter-particle bonding and compressive properties of porous Mo was established.

2. Experimental Procedures

2.1. Preparation of Porous Mo Deposits

Porous Mo deposits with different porosities were prepared through depositing semi-molten Mo particles by flame spraying under different spray conditions. Mo powder with a nominal size range from 50 to 75 μm was used as the starting material. The powder morphology is shown in Figure 1. A stainless steel plate of size 50 × 20 × 3 mm^3 was employed as the substrate. A home-made flame torch was manipulated by a robot to deposit porous Mo. The acetylene flow rate was set at 100, 200, and 300 $L \cdot h^{-1}$, respectively, with a spray distance of 30 mm used to obtain samples with different porosities [24]. The pressures of C_2H_2 and O_2 were fixed at 0.1 and 0.4 MPa, respectively. The deposition was carried out for several passes at a traverse speed of 100 $mm \cdot s^{-1}$ under different spray conditions.

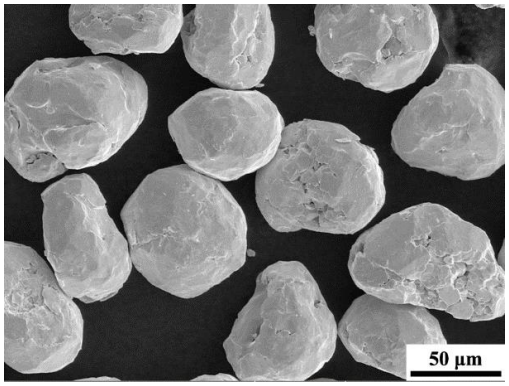

Figure 1. Morphology of the sprayed Mo powder.

2.2. Heat Treatment of Porous Mo

To remove the oxide formed during flame spraying, the as-sprayed porous Mo was placed in a furnace at 1050 °C in an H_2 atmosphere for 2 h. Then, the deposits were placed in a vacuum furnace (MW-L0616V, Changsha Syno-Therm Co. Ltd., Changsha, China) at 1400 °C for 2, 4, and 6 h, respectively, to improve the bonding between the particles. The pressure of the vacuum furnace was set at 10^{-6} Torr.

2.3. Characterization Methods

The morphology and microstructure of porous Mo were characterized via scanning electron microscopy (SEM, FEI QUANTA600F, Waltham, MA, USA and VEGA II-XMU, TSCAN, Brno, Czech Republic). Six SEM cross-sectional images at a magnification of 250 were used for the estimation of the mean porosity of each deposit through image analysis software (Image J, DT200). X-ray diffraction analysis (XRD) was performed using a diffractometer (Rigaku D/Max 2400, Tokyo, Japan) to evaluate the microstructure of the reduced samples. The XRD patterns were collected over a 2θ range from 10° to 90° with a scanning rate of 2°/min. Compression testing was carried out according to the standard for the compressive testing of porous metals (JIS H7902:2008) [9]. Compression test samples with dimensions of $5 \times 5 \times 5$ mm^3 were cut from the substrate by machining. The compressive behavior of porous Mo deposits was tested using universal testing machine (WDW-10 KN, Changchun, China) at a fixed cross-head speed of 0.05 $mm \cdot s^{-1}$.

3. Results and Discussion

3.1. Morphology and Inter-Particle Bonding of As-sprayed Porous Mo Deposits

The surface morphology of the as-sprayed porous Mo and the cross-sectional microstructure of inter-particle bonding are shown in Figure 2. As can be seen from the SEM images in Figure 2a, the porous Mo was stacked by the semi-molten sprayed particles which were bonded by the molten liquid to form a strong particle bonding neck. A dual-scale pore structure can be observed on the surface which includes large holes of a few micrometers and small holes of a few microns. The sheet oxides were on the surface of the Mo particles, as shown in Figure 2a. The cross-sectional microstructure of the inter-particle bonding recorded in back-scattered electron mode is shown in Figure 2b and the corresponding EDS analysis results are shown in Table 1. The results reveal particle bonding necks of different phases according to the image contrast and EDS analysis. Furthermore, the particle bonding neck was quite thick and dense, and the interface between the particle and bonding neck and the interface between the two particles were clearly observed, as seen in the image in Figure 2b. This fact indicated that the particles were in a semi-molten state prior to deposition. During spraying, the Mo particles were divided into two parts: the molten shell on the surface and the unmolten core inside. Obviously, the molten fraction was oxidized by direct contact with the flame. Upon impact

with the solid core of Mo particles, the molten liquid formed oxide shells covering the core [25]. Hence, the oxides were included in the bonding neck and were adhered strongly to the unmolten solid core. The oxidation states were related to the distance between the particle surface and the solid core. On the other hand, the subsequent deposition of particles during the second round of heating may have also lead to an increase in the oxidation degree. However, for the application of the porous metal Mo, the oxide should be removed so that it can form composites with low melting point metals. Therefore, it is necessary to study the performance of reduced porous Mo for the applications of the porous Mo compound with low melting point metals (e.g., Cu).

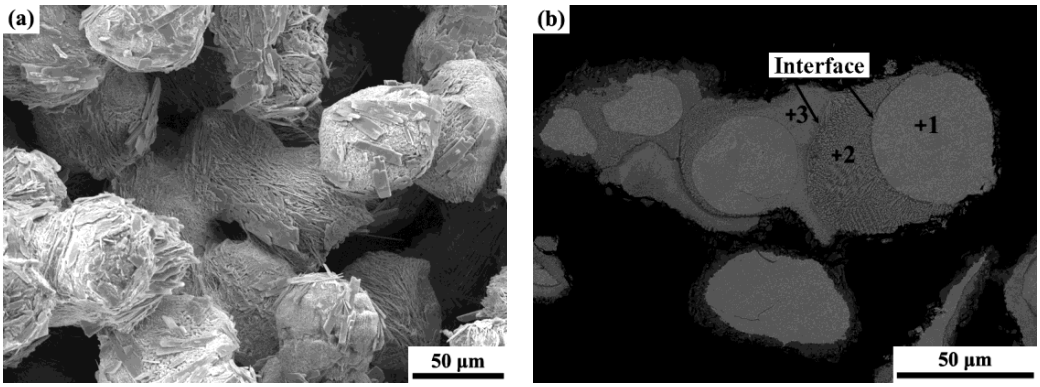

Figure 2. Cross-sectional microstructure of as-sprayed porous Mo surface morphology and inter-particle bonding neck.

Table 1. Chemical compositions of the three points in Figure 2b.

Point	Elemental Composition (wt.%)	
	Mo	O
Point 1	100.00	–
Point 2	63.29	36.71
Point 3	76.63	23.37

3.2. Effect of Reduction on Inter-Particle Bonding of Porous Mo Deposits

The XRD diffraction patterns of the as-sprayed Mo deposits and the reduced porous Mo as obtained under a reduction temperature of 1050 °C in an H_2 atmosphere for 2 h are shown in Figure 3. After heat treatment, the oxides, such as MoO_3, MoO_2, and Mo_4O_{11}, etc., were removed. The main phase in the reduced porous Mo was metallic Mo. These results indicate that the oxides of Mo which were formed during the flame spraying process can be efficiently removed under these reduction conditions.

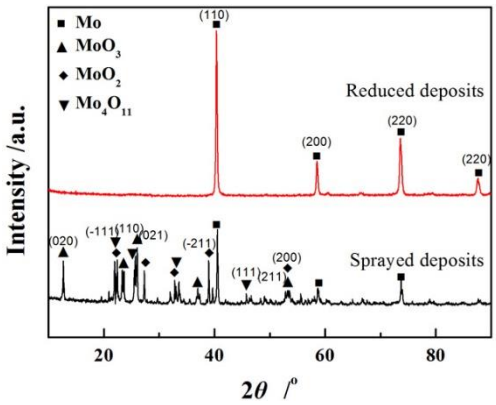

Figure 3. X-ray diffraction (XRD) diffraction patterns of sprayed and reduced porous Mo.

Figure 4 shows the surface morphology of the porous Mo in (a,b) and the cross-sectional morphology of the inter-particle bonding neck (c,d) after heat treatment. A clear change in appearance was observed after the reduction. The sheet oxides disappeared and many tiny particles and pore structures were distributed on the surface of the semi-molten particles. During the reduction, the oxygen volatilization resulted in volume shrinkage and micropore formation. The bonding neck between the two particles became loose and porous after reduction, as shown in Figure 4c,d. It was found that the inside of the bonding neck was also porous after reduction treatment. It is well known that inter-particle bonding can be improved by sintering treatment due to grain growth and densification. Thus, the results indicate that the sintering of the bonding neck was insufficient because the heat treatment temperature (1050 °C) was much lower than the melting point of Mo (2600 °C). It can be inferred that the oxides of the bonding neck shrank due to the volatilization of the reduction product and the compressive strength of the bonding neck reduced as the density decreased. Therefore, in order to improve inter-particle bonding and achieve complete sintering of the bonding neck, the heating should be performed at a higher temperature or for a longer time.

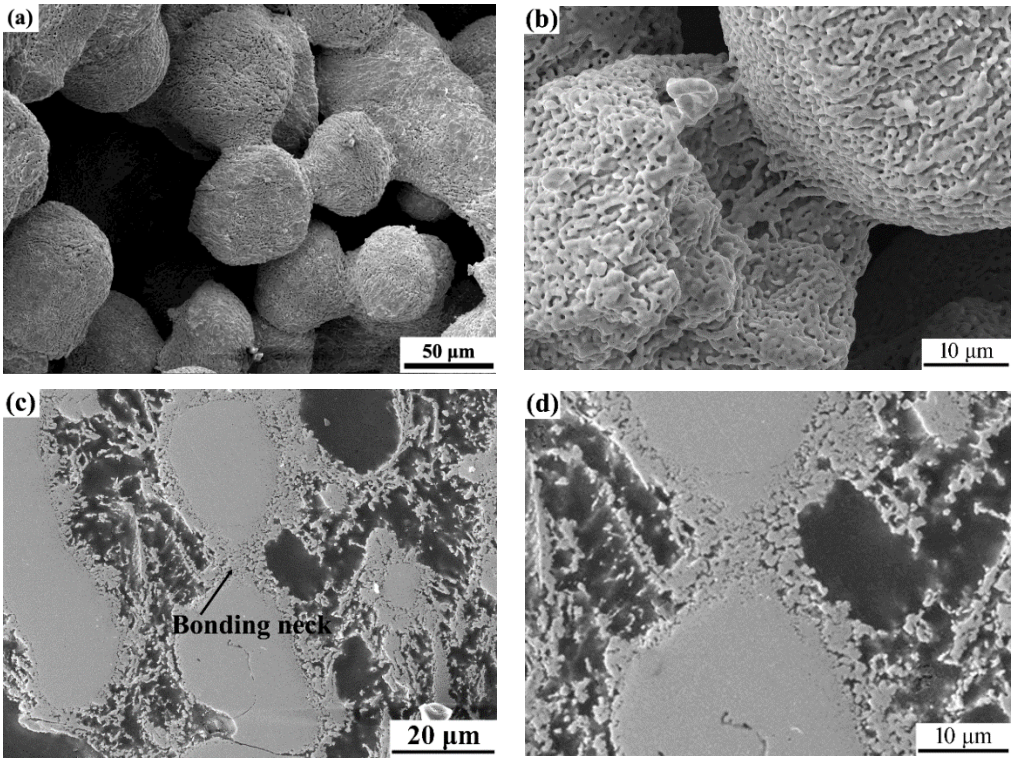

Figure 4. Surface morphology of reduced porous Mo (**a**,**b**) and cross-sectional microstructure of inter-particle bonding neck (**c**,**d**).

3.3. Effect of Sintering on Inter-Particle Bonding of Porous Mo Deposits

In order to study the effect of sintering on inter-particle bonding, the reduced porous Mo was sintered in a vacuum furnace at a sintering temperature of 1400 °C and sintering durations of 2, 4, and 6 h, respectively. The surface morphology of the porous Mo and the cross-sectional morphology of the bonding neck at the sintering times of 2 and 6 h are shown in Figure 5a,b and Figure 5c,d, respectively. From the microporous structure image, it is clear that the surface of the Mo particles became significantly smoother after 6 h of sintering. This was mainly because the high temperature sintering process caused the Mo particles to grow and fuse together. However, many residual micropores were still observed on the surface of the particles. This indicates that the sintering effect was limited under the present heat treatment conditions. Although the surface of the inter-particle bonding neck became smooth in Figure 5a, few micropores still existed in the bonding neck area,

as shown in Figure 5b. It can be inferred that the bonding between particles can be effectively improved by controlling the sintering temperature and sintering time.

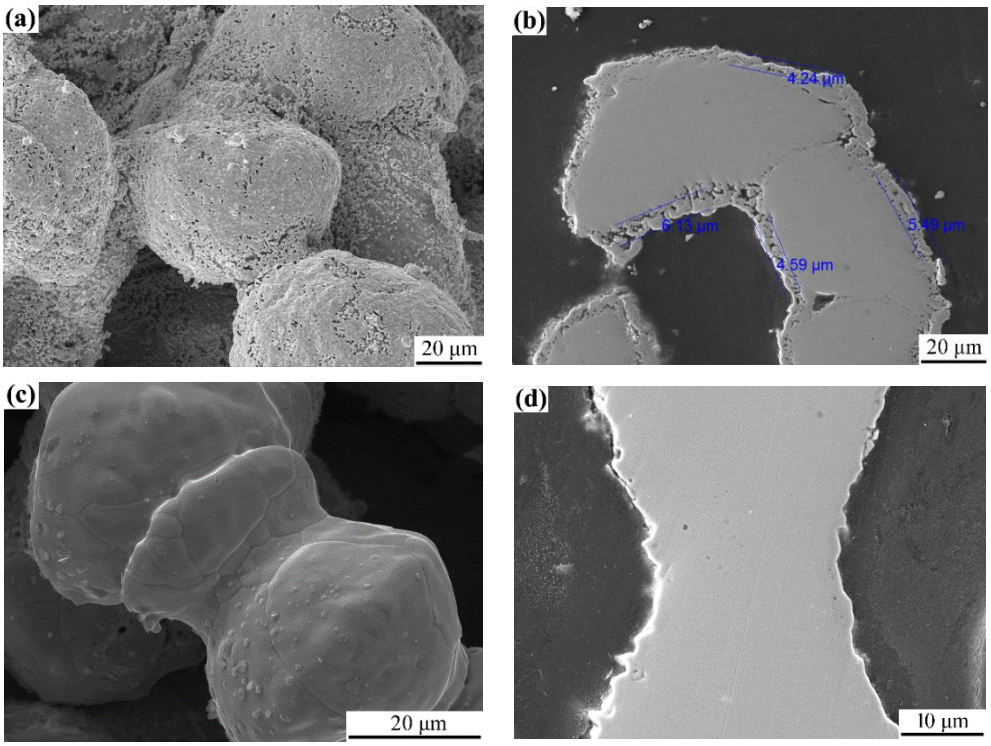

Figure 5. Surface morphology of porous Mo and cross-sectional microstructure of inter-particle bonding neck for sintering times of 2 h (**a**,**b**) and 6 h (**c**,**d**), respectively.

3.4. Compression Properties of Porous Mo Deposits

3.4.1. Compression Properties of As-sprayed Porous Mo Deposits

The compression stress-strain curve of as-sprayed porous Mo deposits is shown in Figure 6. The porosity levels of the three samples were 50% (Curve 1), 60% (Curve 2) and 68% (Curve 3), respectively. With the increase in strain, the curves displayed three distinct regions: the elastic deformation stage, the deformation plateau stage, and the densification stage, similarly to the previous report [12]. In the elastic deformation stage, stress increased almost linearly with strain, up to 10%. Generally, during this stage deformation can be restored when the stress is removed, and thus it is called the elastic deformation stage. When the sample porosity was about 68%, stress increased much slower with the increase in strain as compared to the samples with porosities of 60% and 50%. The maximum compressive strengths of the porous Mo deposits were 103, 40, and 22 MPa when the porosity levels were 50%, 60%, and 68%, respectively. This result is possibly due to a large bonding neck close to the original diameter of the particles between the adjacent particles, due to metallurgical bonding. Moreover, the bonding necks between semi-molten particles gradually diminished with the increase in porosity of the porous Mo deposits because the melting degree of the particles decreased [9]. When the elastic deformation stage ends stress increases much less and even tends to decrease with large strain; this is referred to as the deformation plateau stage. However, the deformation plateau stages of the stress-strain curves showed unstable characteristics, which was probably due to the dual-scale pore structure of the porous deposit. It may be concluded that the deformation and collapse of the bonding neck between particles occurred in the porous deposit. As the porosity reached 50%, 60%, and 68%, the mean platform stresses were about 55.5, 32.4, and 19.6 MPa, respectively. Subsequently, the porous deposits became gradually denser with a further increase in stress as the strain increased up to 50%.

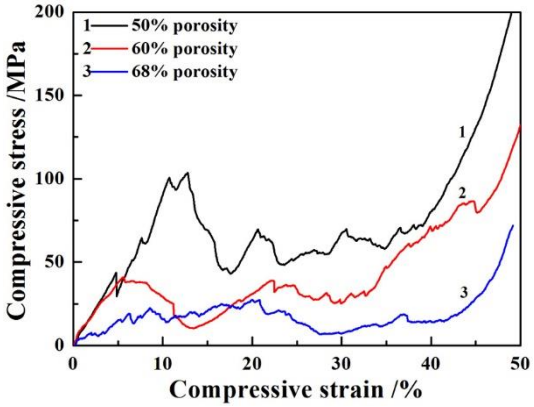

Figure 6. Compressive stress-strain curves of as-sprayed porous Mo deposits with different porosities.

3.4.2. Influence of Reduction on Compression Properties of Porous Mo Deposits

In Figure 7, Curves 1 and 2 show the compressive stress-strain curves of as-sprayed and reduced porous Mo deposits with 50% porosity after heat treatment at 1050 °C under a hydrogen atmosphere for 2 h, respectively. The porosity value of the porous Mo deposit was 50%. It can be seen that the compression stress-strain curve of the porous Mo consisted of three stages. In particular, the reduction curve of the stress platform area, following heat treatment, became almost level. The compressive strength of the sprayed porous Mo (Curve 1) showed three peaks at about 43, 63 and 103 MPa, respectively, during the elastic deformation stage. In addition, several intense peaks were observed during the deformation plateau stage. These were probably due to the inter-particle bonding formed by the brittle oxide, as mentioned earlier. After the heat treatment, the compressive yield strength of the porous Mo decreased significantly to 1/10th of the sprayed sample, as shown in Curve 2. However, after two hours of reduction heat treatment, the compression stress-strain curve of the porous Mo became smooth and an extended deformation plateau stage was observed. The mean platform stress was about 10.68 MPa. On one hand, the brittle oxidation of particles the during spraying process was reduced under an H_2 atmosphere at 1050 °C. Hence, the toughness of the sample was enhanced, and the stress-strain curve was smooth. On the other hand, after the reduction process, oxidation shrinkage made the inter-particle bonding neck loose and porous. Thus, the stress strength decreased markedly. Furthermore, after the reduction process, the corresponding variables of the elastic deformation stage of the curve were reduced significantly. This indicates that the sample brittleness was more significant. Although the porosity values of the two samples were similar, the stress strengths of the as-sprayed and reduced porous Mo deposits were very different. It can be inferred that the compression performance of the deposit fabricated by semi-molten particles was mainly dependent on inter-particle bonding.

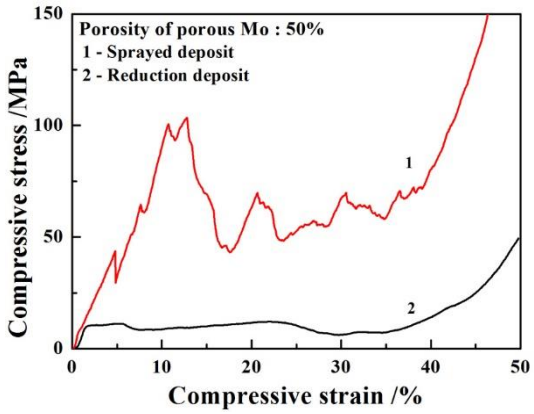

Figure 7. Compressive stress-strain curves of as-sprayed and reduced porous Mo deposits with 50% porosity.

3.4.3. Influence of Sintering on Compression Properties of Porous Mo Deposits

It is well known that during the sintering process, hold time and temperature have a significant effect on combination between particles. Therefore, in order to understand the relationship between inter-particle bonding and compressive strength, the reduced porous Mo was placed in a vacuum furnace for sintering for 2, 4, and 6 h, respectively. The compressive stress-strain curves of reduced porous Mo with a porosity of 50% after sintering are shown in Figure 8. It was found that the compressive strength increased from 23 to 40 to 53 MPa as the sintering time increased. When the treatment time was only 2 h, the compressive strength was still higher than that of the sample after reduction. When the sintering time was extended to 6 h, the value of the compressive strength was nearly the mean platform stress of the sprayed sample. The elastic deformation stage made up almost 10% of the strain value, which was the same as that for the as-sprayed porous Mo deposit. Moreover, the sintering process produced the appearance of two stages in the curve of deformation plateau stage. When the elastic deformation stage ended, the platform stress value corresponded to the maximum compressive strength until the strain was around 20% to 25%. Then, the compressive stress value sharply reduced by about half. This was possibly due to the dual-scale pore structure of the porous deposit. Therefore, with the increase in strain, some large pores collapsed first, causing the compressive stress value to decrease significantly. Subsequently, the compressive stress value remained steady until the small holes collapsed and entered into the densification stage. These results again demonstrated that the sintering of porous Mo was promoted by prolonging the treatment time because the inter-particle bonding was improved. As a result, the compression performance increased at the same porosity.

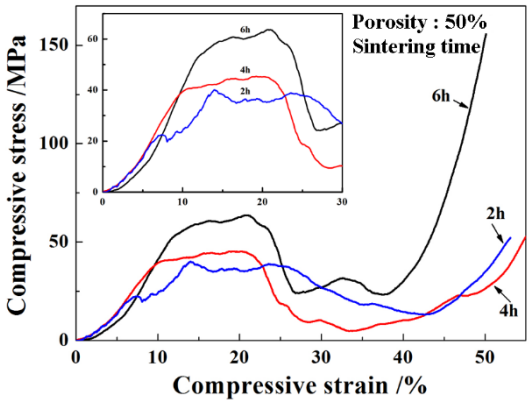

Figure 8. Effect of sintering time on the compressive stress-strain curves for porous Mo deposits with 50% porosity.

4. Conclusions

In this study, porous Mo was fabricated through the deposition of semi-molten spray particles by flame spraying. It is generally accepted that the compressive properties of porous materials mainly depends on porosity. However, it has been found that the inter-particle bonding neck has an important effect on the compressive properties of porous materials. To understand this, the compressive properties of porous Mo and the corresponding inter-particle bonding neck were investigated based on as-sprayed, reduced, and sintered porous Mo deposits. The main results are outlined here. With increase in strain, the compressive stress-strain curves of porous Mo deposits displayed three characteristic regions: the elastic deformation stage, the deformation plateau stage, and the densification stage. The maximum compressive strengths of the porous Mo deposits were 103, 40, and 22 MPa when the sample porosities were 50%, 60%, and 68%, respectively. The deformation plateau stage of the as-sprayed porous Mo deposits was unstable. This was due to the concentrating melt at the impact of semi-molten spray particles which formed metallurgical bonding with a large

bonding neck with the underlying particle; inter-particle bonding was formed by the brittle oxides. The oxides of Mo formed during the flame spraying process were efficiently removed by heating at 1050 °C under an H_2 atmosphere. The compression stress-strain curve of porous Mo with 50% porosity became smooth and showed an extended deformation plateau stage. The mean platform stress was about 10.68 MPa due to the inter-particle bonding neck becoming porous and tough after reduction. The compressive strengths of the porous Mo deposits were 23, 40, and 53 MPa at sintering times of 2, 4, and 6 h, respectively. Heat treatment at 1400 °C caused secondary sintering. As the sintering time was extended, the porous inter-particle bonding neck became denser. Thus, the bonding between the particles was improved, which led to improvements in the compression properties. Therefore, it can be inferred that the inter-particle bonding and compressive properties of flame-sprayed porous Mo can be significantly improved by optimizing the sintering temperature and the heat treatment time.

Author Contributions: Conceptualization, J.Y.; Data Curation, J.Y.; Formal Analysis, Y.L.; Investigation, J.Y.; Methodology, H.D.; Resources, X.L.; Writing—Original Draft, J.Y.; Writing—Review and Editing, Y.L.; Validation, H.D.; Supervision, Y.L. and X.L.

Funding: The research was funded by the Natural Science Foundation Research Project of Shaanxi Province (No. 2017JQ5042), the Special Research Program Department of Education of Shaanxi Province (No. 17JK0612), and the Materials Science and Engineering of Provincial Advantage Disciplines of Xi'an Shiyou University (No. YS37020203).

Acknowledgments: The guidance and help of Changjiu Li from Xi'an Jiaotong University.

Conflicts of Interest: The authors declare no conflict of interest.

References

1. Zhao, B.; Yu, T.Y.; Ding, W.F.; Zhang, L.C.; Su, H.H.; Chen, Z.Z. Effect of micropores on the microstructure and mechanical properties of porous Cu-Sn-Ti composites. *Mater. Sci. Eng. A* **2018**, *730*, 345–354. [CrossRef]
2. Li, B.Q.; Wang, C.Y.; Lu, X. Effect of pore structure on the compressive property of porous Ti produced by powder metallurgy technique. *Mater. Des.* **2013**, *50*, 613–619. [CrossRef]
3. Cao, Y.J.; Shen, W.Q.; Shao, J.F.; Burlion, N. Influences of micro-pores and meso-pores on elastic and plastic properties of porous materials. *Eur. J. Mech. A. Solids* **2018**, *72*, 407–423. [CrossRef]
4. Okulov, I.V.; Volegov, A.S.; Markmann, J. Tuning microstructure and mechanical properties of open porous TiNb and TiFe alloys by optimization of dealloying parameters. *Scr. Mater.* **2018**, *154*, 68–72. [CrossRef]
5. Segurado, J.; Parteder, E.; Plankensteiner, A.F.; Bohm, H.J. Micromechanical studies of the densification of porous molybdenum. *Mater. Sci. Eng. A* **2002**, *333*, 270–278. [CrossRef]
6. Jaworski, M.A.; Lau, C.Y.; Urbansky, D.L.; Malfa, M.B.; Gray, T.K.; Neumann, M.J.; Ruzic, D.N. Observations of liquid lithium uptake in a porous molybdenum foam. *J. Nucl. Mater.* **2008**, *378*, 105–109. [CrossRef]
7. Narayanasamy, R.; Ponalagusamy, R.; Subramanian, K.R. Generalised yield criteria of porous sintered powder metallurgy metals. *J. Mater. Process. Technol.* **2001**, *110*, 182–185. [CrossRef]
8. Yao, J.T.; Li, C.J.; Li, Y.; Chen, B.; Huo, H.B. Relationships between the properties and microstructure of Mo–Cu composites prepared by infiltrating copper into flame-sprayed porous Mo skeleton. *Mater. Des.* **2015**, *88*, 774–780. [CrossRef]
9. Yao, J.T.; Yang, G.J.; Li, C.X.; Li, C.J. Fabrication of porous stainless steel by flame spraying of semimolten particles. *Mater. Manuf. Process.* **2014**, *29*, 1253–1259. [CrossRef]
10. Bai, C.Y.; Colombo, P. Processing, properties and applications of highly porous geopolymers: A review. *Ceram. Int.* **2018**, *44*, 16103–16118. [CrossRef]
11. Qin, J.H.; Chen, Q.; Yang, C.Y.; Huang, Y. Research process on property and application of metal porous materials. *J. Alloy. Compd.* **2016**, *654*, 39–44. [CrossRef]
12. Yiatros, S.; Marangos, O.; Votsis, R.A.; Brennan, F.P. Compressive properties of granular foams of adhesively bonded steel hollow sphere blocks. *Mech. Res. Commun.* **2018**, *94*, 13–20. [CrossRef]
13. Zhou, W.; Tang, Y.; Liu, B.; Song, R.; Jiang, L.L.; Hui, K.S.; Hui, K.N.; Yao, H.M. Compressive properties of porous metal fiber sintered sheet produced by solid-state sintering process. *Mater. Des.* **2012**, *35*, 414–418. [CrossRef]

14. Li, F.; Li, J.; Xu, G.; Liu, G.; Kou, H.; Zhou, L. Fabrication, pore structure and compressive behavior of anisotropic porous titanium for human trabecular bone implant applications. *J. Mech. Behav. Biomed. Mater.* **2015**, *46*, 104–114. [CrossRef] [PubMed]
15. Liu, J.A.; Shi, S.Q.; Zheng, Z.B.; Huang, K.; Yan, Y.Y. Characterization and compressive properties of Ni/Mg hybrid foams. *Mater. Sci. Eng. A.* **2017**, *708*, 329–335. [CrossRef]
16. Liu, Y.J.; Wang, H.L.; Li, S.J.; Wang, S.G.; Wang, W.J.; Hou, W.T.; Hao, Y.L.; Yang, R.; Zhang, L.C. Compressive and fatigue behavior of beta-type titanium porous structures fabricated by electron beam melting. *Acta Mater.* **2017**, *126*, 58–66. [CrossRef]
17. Qiao, J.C.; Xi, Z.P.; Tang, H.P.; Wang, J.Y.; Zhu, J.L. Influence of porosity on quasi-static compressive properties of porous metal media fabricated by stainless steel fibers. *Mater. Des.* **2009**, *30*, 2737–2740. [CrossRef]
18. Zou, C.M.; Liu, Y.; Yang, X.; Wang, H.W.; Wei, Z.J. Effect of sintering neck on compressive mechanical properties of porous titanium. *Trans. Nonferr. Met. Soc. China* **2012**, *22*, 485–490. [CrossRef]
19. Gu, D.D.; Shen, Y.F. Processing conditions and microstructural features of porous 316L stainless steel components by DMLS. *Appl. Surf. Sci.* **2008**, *255*, 1880–1887. [CrossRef]
20. Takata, N.; Uematsu, K.; Kobashi, M. Compressive properties of porous Ti–Al alloys fabricated by reaction synthesis using a space holder powder. *Mater. Sci. Eng. A.* **2017**, *697*, 66–70. [CrossRef]
21. Vesenjak, M.; Kovačič, A.; Tane, M.; Borovinšek, M.; Nakajima, H.; Ren, Z. Compressive properties of lotus-type porous iron. *Comput. Mater. Sci.* **2012**, *65*, 37–43. [CrossRef]
22. Lin, J.G.; Li, Y.C.; Wong, C.S.; Hodgson, P.D.; Wen, C.E. Degradation of the strength of porous titanium after alkali and heat treatment. *J. Alloy. Compd.* **2009**, *485*, 316–319. [CrossRef]
23. Salahinejad, E.; Amini, R.; Marasi, M.; Hadianfard, M.J. The effect of sintering time on the densification and mechanical properties of a mechanically alloyed Cr–Mn–N stainless steel. *Mater. Des.* **2010**, *31*, 527–532. [CrossRef]
24. Chen, B.; Li, C.J.; Yang, G.J.; Yao, J.T.; Huo, H.B.; Li, C.X. Fabrication of porous molybdenum by controlling spray particle state. *J. Therm. Spray Technol.* **2012**, *21*, 1032–1045. [CrossRef]
25. Yao, J.T.; Ren, J.Q.; Hui, B.H.; Yang, G.J.; Li, C.X.; Li, C.J. Deposition behavior of semi-molten spray particles during flame spraying of porous metal alloy. *J. Therm. Spray Technol.* **2014**, *23*, 991–999. [CrossRef]